Structural anisotropy and internal magnetic fields in trabecular bone: Coupling solution and solid dipolar interactions

Louis-S. Bouchard [a], Felix W. Wehrli [b], Chih-Liang Chin [b], Warren S. Warren [a],*

[a] *Department of Chemistry, Princeton University, Princeton, NJ 08544, USA*
[b] *Department of Radiology, University of Pennsylvania, Philadelphia, PA 19104, USA*

Abstract

We investigate the use of intermolecular multiple-quantum coherence to probe structural anisotropy in trabecular bone. Despite the low volume fraction of bone, the bone–water interface produces internal magnetic field gradients which modulate the dipolar field, depending on sample orientation, choice of dipolar correlation length, correlation gradient direction, and evolution time. For this system, the probing of internal magnetic field gradients in the liquid phase permits indirect measurements of the solid phase dipolar field. Our results suggest that measurements of volume-averaged signal intensity as a function of gradient strength and three orthogonal directions could be used to non-invasively measure the orientation of structures inside a sample or their degree of anisotropy. The system is modeled as having two phases, solid and liquid (bone and water), which differ in their magnetization density and magnetic susceptibility. A simple calculation using a priori knowledge of the material geometry and distribution of internal magnetic fields verifies the experimental measurements as a function of gradient strength, direction, and sample orientation.
© 2005 Elsevier Inc. All rights reserved.

1. Introduction

The potential of intermolecular multiple-quantum coherence in non-invasively probing material microstructure in liquid state NMR has been acknowledged [1–3]. Pulse sequences exist that generate signals which are proportional to the strength of the distant dipolar field (DDF) [1]. These signals can be spatially resolved, as in the case of magnetic resonance imaging, or can be averaged over larger regions—or voxels—to provide high signal-to-noise bulk measurements. In both cases, the localized or unlocalized signals encode information about the material microstructure and its underlying geometry.

Biphasic materials modeled with a solid phase that does not contribute to the measured signal, and a NMR-sensitive liquid phase that encodes the geometry of the solid phase, are of interest to the biomedical and materials sciences. It was recently shown [4] that the volume-averaged DDF can be decoded to reconstruct simple material geometries. Thus, bulk measurements of the DDF would constitute imaging experiments in their own right, with the added advantages that sensitivity is not lost by having to use smaller imaging voxels and structural information below the voxel size can be obtained. It was also shown [5,3,6] that spatially resolved measurements in imaging experiments can remotely detect changes in magnetization density

* Corresponding author. Fax: +1 609 258 6746
 E-mail address: wwarren@princeton.edu (W.S. Warren).

occurring at distances beyond the size of the imaging voxel. These changes can, moreover, be quantitatively predicted by theory [5]. Beyond porous materials, the method has found applications in functional imaging [7], tumor detection [8,9], and amplification of weak NMR signals [10,11].

Most studies to date have focused on magnetization density differences in a structured material and their effects on modulating the DDF, while the effects of internal magnetic field gradients remain poorly characterized. Internal field gradients can be useful in tumor detection [8,9], functional imaging [7], and also for structural studies in the case where a large enough susceptibility difference exists between the phases of a material but the volume fraction of the solid phase is too low to modulate the DDF significantly. The present article studies the DDF dependence of trabecular bone on pulse sequence parameters and sample orientation. The bone volume fraction is typically 14% or less, while the water and bone phases differ significantly in their magnetic susceptibilities (by 2.28 ppm): pure water has a magnetic susceptibility of −9.03 ppm in SI (système international) units while the solid phase of trabecular bone is at −11.31 ppm. See Hopkins and Wehrli [12].

Trabecular bone consists essentially of an array of interconnected struts and plates arranged in such a fashion as to optimally withstand the stresses to which it is subjected. The structural elements are aligned with the major stress lines, forming a structurally anisotropic network [13]. The internal magnetic field gradients that are generated by the interface of the two phases offer the possibility of further characterizing the geometry. To assess the feasibility of modeling trabecular bone, we are interested in knowing the dependence of the DDF on sample orientation and internal magnetic field gradients. Such modeling, if it could lead to a reliable method for probing architectural parameters, would be of clinical interest since bone loss, as it occurs in postmenopausal osteoporosis or extended exposure to microgravity, is associated with architectural changes that include anisotropy. For example, it is known that trabecular bone becomes more anisotropic through preferential loss of transverse trabeculae (i.e., those perpendicular to the loading direction), therefore making the bone more prone to failure by buckling.

Other examples of anisotropic biological materials include neural fiber and capillary networks. In many cases where MRI and other imaging modalities cannot spatially resolve the structures, alternative methods which non-destructively probe the structural integrity of complex heterogeneous materials are needed.

In this article, we investigate the dependence of NMR measurements of the magnetic DDF on gradient strength and direction, evolution time, and sample orientation. This functional dependence in specimens of trabecular bone shows a strong sensitivity to trabecular orientation with respect to the gradient direction, thus offering new possibilities for using this technique in monitoring microstructural anisotropy and integrity of porous materials. We find that a linear model for the time expansion of the magnetization evolution is adequate for calculating DDF-dependent signals and corroborates experimental measurements in our system of trabecular bone in which the marrow was replaced by water as the NMR-active medium.

1.1. Calculating the CRAZED signal

The three-dimensional biphasic medium is described in terms of the indicator function $\chi(\mathbf{r})$ of the fluid phase $\Omega \in \mathbb{R}^3$ [4], which equals 1 when $\mathbf{r} \in \Omega$ and 0 otherwise (i.e., $\chi(\mathbf{r})$ is the simple "step" function that takes the value 1 when the vector $\mathbf{r}$ points to the liquid region and equals 0 when $\mathbf{r}$ points elsewhere). Since the solid phase generally differs in magnetic susceptibility, we must specify the susceptibility shift, which in turn determines the distribution of resonance frequency offsets $\omega(\mathbf{r})$. $\omega(\mathbf{r})$ therefore provides an indirect measurement of the coupling between the liquid phase magnetization and the dipole field of the solid phase. $\omega(\mathbf{r})$ can be directly measured by high-resolution MRI [14], or may be calculated either by summing the dipoles of the solid phase, or equivalently, by adding the individual fields from induced surface charge elements [15].

For a double-quantum CRAZED sequence, consisting of preparation and detection periods [1,9], and with conditions of weak DDF encountered in most clinical experiments, the expected CRAZED signal is most conveniently calculated in the linear approximation, where the signal intensity is directly proportional to the DDF. See Ramanathan and Bowtell [3] for the conditions of validity of this regime.

Insight pertaining to the behavior of DDF measurements can be gathered by solving the forward problem which consists of calculating the expected CRAZED signal for a given geometry and distribution of local magnetic fields and comparing to the experimental measurements. Also of interest are solutions to the inverse problem for reconstructing the material geometry from DDF measurements [4]. The inverse problem is not treated in this study, but could be addressed by extending the reconstruction method [4] with the addition of a DDF calculation which models the solid phase and its altering of the resonance frequency distribution over the liquid phase.

The primary role of the forward problem is to validate the experimental measurements by confirming the various trends observed. These trends, as will be seen later, reveal that the method is highly sensitive to internal magnetic field gradients over specific length scales and this dependence suggests a potentially useful tool for probing the architecture of trabecular bone or other

oriented materials. As mentioned previously, the two essential ingredients for the calculation are the (1) the indicator function $\chi(\mathbf{r})$ and (2) spatial distributions of resonance frequency $\omega(\mathbf{r})$. The functions $\chi(\mathbf{r})$ and $\omega(\mathbf{r})$ were both derived from high-resolution MRI of the bone sample; the experimental procedure for doing this is detailed in Section 3.

For the CRAZED preparation shown in Fig. 1 with flip angles $\beta_1 = \pi/2$ and $\beta_2 = 2\pi/3$, the magnetization evolution due to RF pulses approximated by infinitely short rotations, correlation gradients, and local resonance frequency offsets incurred from $t = 0$ up to time $t = \tau/2 + \tau/2 + \tau + \tau$ is calculated by application of rotation matrices to the equilibrium magnetization $\vec{M}_0(\mathbf{r}) = M_{eq}\chi(\mathbf{r})\hat{\mathbf{z}}$. Or equivalently, Eq. (5.7) of [16] can be used to calculate the magnetization distribution $\vec{M}_t(\mathbf{r})$.

By discretizing $\omega(\mathbf{r})$ and $\chi(\mathbf{r})$ on a cubic grid of 128^3 evenly spaced points, we calculate the components of the bulk NMR signal at time $t = \tau/2 + \tau/2 + \tau + \tau$ (we neglect the spin echo acquisition for this calculation; it is used in practice mainly to allow the CRAZED signal to grow in) for a given value of the evolution time τ and gradient wave vector $\mathbf{k}$ using the volume integral in discrete form $\sum_{\mathbf{r}_l \in \Omega} M_{t,j}(\mathbf{r}_l)B_k(\mathbf{r}_l) - M_{t,k}(\mathbf{r}_l)B_j(\mathbf{r}_l)$, where $M_{t,k}(\mathbf{r}_l)$ is the magnetization after CRAZED evolution, including gradient pulse modulations and phase accrued due to $\omega(\mathbf{r})$; $B_j(\mathbf{r}_l)$ is the corresponding DDF acting on $M_{t,k}(\mathbf{r}_l)$.

The components of the DDF are calculated by doing a discrete Fourier transformation of the magnetization $\vec{M}(\mathbf{r}) \rightarrow \tilde{M}(\mathbf{k})$ and use of the well-known expression [17] $\tilde{B}(\mathbf{k}_i) = \frac{4\pi}{6}[3\tilde{M}_z(\mathbf{k}_i)\hat{\mathbf{z}} - \tilde{M}(\mathbf{k}_i)][1 - 3(\hat{\mathbf{k}}_i \cdot \hat{\mathbf{z}})^2]$, where $\mathbf{k}_i$ runs over the entire grid and $\hat{\mathbf{k}}_i$ is the unit vector $\mathbf{k}_i/|\mathbf{k}_i|$. This operation is followed by inverse Fourier transformation $\tilde{B}(\mathbf{k}) \rightarrow \vec{B}(\mathbf{r})$.

The calculation is repeated for several values of the wave vector, ranging from wavelengths of 4 to 56 grid
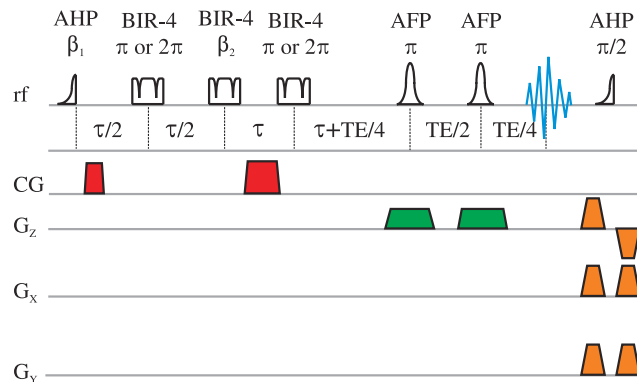

Fig. 1. Timing diagram of the iDQC CRAZED pulse sequence with adiabatic pulses. The CRAZED or MODCRAZED preparation is followed by a spin echo detection. Each RF pulse has a fixed duration of 2 ms. The correlation gradient (CG) pulses, in 2:1 ratio of areas, are applied along x, y or z. Pulse waveforms: adiabatic half-passage (AHP), adiabatic full-passage (AFP), B_1-insensitive plane rotation (BIR-4) (see Garwood and DelaBarre [21]).

points in steps of 4, which corresponds approximately to correlation distances d_c in the range 200 μm to 7 mm. For each run, the signal is phase cycled using a four-step scheme: the first RF pulse phase is $\phi = (0, \pi, \pi/2, 3\pi/2)$ while the receiver phase is $(0, 0, \pi, \pi)$. These calculations were implemented in the C language on Pentium IV machines.

The MODCRAZED ("modified" CRAZED) [18] experiment is a variant of the CRAZED preparation with a refocusing π pulse at the center of the evolution period reversing the phase evolution from local resonance frequency offsets. It is used to determine the contribution of resonance frequency offsets to the bulk signal decay (details in next section). In cases where diffusion effects are negligible, this is formally equivalent to setting $\omega(\mathbf{r}) \equiv 0$. With the pulse sequence in Fig. 1, MODCRAZED is achieved by using the π pulse rather than the 2π pulse (the 2π pulse is a dummy pulse to provide easy switching to the CRAZED signal).

2. Experimental protocol

A trabecular bone specimen from the human distal tibia was cut into a cylindrical core of approximately 2.8 cm diameter and 2 cm length. After removal of bone marrow the core was suspended in water. The sample was placed in a 3 cm diameter, 4 cm long cylindrical plastic container, with the cylinder axis parallel to the axis of the tibia. The preparations were done in a water bath to minimize the amount of air bubbles into the tube. The core was wrapped in a layer of parafilm which provided a tighter fit to the container tube, restricting motion.

NMR measurements were made using two different instruments. In the first setup, we used a 4T whole-body MRI scanner (GE Signa Echospeed 5.7) at the University of Pennsylvania with a home-built solenoid probe with long axis perpendicular to B_0 and the principal axis of the trabeculae perpendicular to B_0 (Fig. 2A). The trabecular orientation can be described in terms of a "fabric tensor." See Harrigan and Mann [19]. The cylinder axis is parallel to the bone's anatomic axis. The principal eigenvector of the fabric tensor roughly coincides with the anatomic axis of the bone.

In the second setup, we used a 7T horizontal-bore animal MRI scanner equipped with a Bruker console and 3 cm diameter birdcage coil aligned along B_0 (Fig. 2B). We will refer to these two configurations as Setup #1 and Setup #2, respectively; they allow the sample to be aligned with the principal axis of the trabeculae perpendicular or parallel to B_0, as illustrated in Fig. 2.

On the Bruker system we used the hybrid CRAZED/MODCRAZED sequence shown in Fig. 1. Adiabatic pulses were used to provide better excitation and
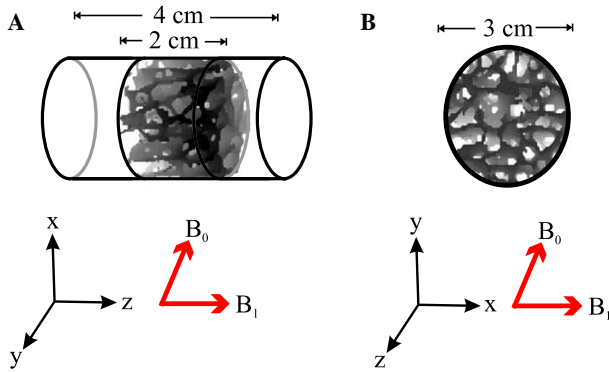
Fig. 2. Coordinate conventions describing two orientations of the bone specimen. (A) Setup #1 has principal axis (see text for details) z of trabeculae perpendicular to B_0. (B) Setup #2 has it parallel to B_0. In both cases, the slice axis is along z and the 1 cm thick slice is centered on the sample.

accurate flip angles. The preparation period for a CRAZED measurement is the following sequence of pulses and delays:

$$\mathcal{R}(\beta_1) - \frac{\tau}{2} - \mathcal{R}(2\pi) - \frac{\tau}{2} - GT - \mathcal{R}(\beta_2) - 2GT - \tau$$
$$- \mathcal{R}(2\pi) - \tau,$$

where $\mathcal{R}(\theta)$ denotes a rotation (RF pulse) by angle θ. The flip angles are $\beta_1 = \pi/2$ and $\beta_2 = 2\pi/3$. $2GT$ and GT are the correlation gradients in ratio 2:1. (For clarity, RF and gradient pulses have zero duration in the above sequence; the actual delays are shown in Fig. 1.) This preparation is followed by the detection sequence:

$$\frac{TE}{4} - \mathcal{R}(\pi) - \frac{TE}{2} - \mathcal{R}(\pi) - \frac{TE}{4} - \text{acquire.}$$

The spin echo acquisition with TE delay allows the CRAZED signal to grow in [20]. Magic angle crusher pulses conclude the preparation/acquisition by nulling the average magnetization prior to the next acquisition [9]. This hybrid sequence conveniently allowed switching from CRAZED to MODCRAZED [18] mode by simply replacing the $\beta_2 = 2\pi/3$ by $\beta_2 = \pi/3$ and the 2π pulse by π. The BIR-4 [21] plane rotation π and 2π pulses, with their identical amplitude modulation waveforms, result in the same amount total RF power deposited in the CRAZED and MODCRAZED experiments.

Selection of 1 cm thick slices is performed using a pair of slice-selective hyperbolic secant refocusing pulses. The bulk signal from the entire slice is sampled by averaging 10 points (spectral width: 50 kHz) at the center of the echo. Repetition time of all sequences was set to 5 s. Echo times are reported as *effective* echo times, $TE_{eff} = TE + 2\tau$; keeping TE_{eff} fixed results in the same amount of T_2 evolution following the β_2 pulse. In all cases, the four-step phase cycle was used. On the GE system, the sequence is identical except for the absence of 2π pulses.

3. Results

In a control experiment, a 3 cm diameter cylindrical plastic tube was filled with water; CRAZED and MOD-CRAZED signals were measured as function of correlation distance d_c and the three orthogonal gradient directions x, y, and z. Results are shown in Fig. 3. In the left column, Figs. 3A and C are plots of the raw signal magnitude versus correlation distance. We observe that the z gradient curves have twice the magnitude of the x or y gradients, as we would expect from a signal which arises from the DDF [9]. At very short correlation distances signal decay is observed as the diffusion weighted regime is approached. (The diffusion regime has been studied by Ramanathan and Bowtell [22].) As the correlation distance is increased the curves remain flat, but decay very slowly with increasing d_c. This decay appears to be due to the finite size of the sample tube; additional experiments done with tubes of a smaller diameter show more rapid decay (data not shown). The z gradient curves have decay slopes twice as large as for the x and y gradients. However, this overall scaling is also due to the DDF weighting and is eliminated by normalizing the curves to the first point, as shown in the right column, in Figs. 3B and D. The decay is slightly more rapid for the CRAZED experiment (Fig. 3B) compared to MODCRAZED (Fig. 3D). We attribute this additional decay to the macroscopic variations in the static field; when we discuss Fig. 8 we show that shimming perturbs the decay slightly. To compare relative changes, all subsequent plots are normalized to the first point unless otherwise specified.

In Figs. 4A and B are the measured signal intensities (magnitude) for the bone specimen versus correlation distance and gradient direction for a MODCRAZED and CRAZED sequence. The MODCRAZED curves resemble those for the pure water sample, as expected for a sample whose magnetization density distributions are isotropic or where the solid phase has a low volume fraction. For these bone samples we calculated the bone volume fraction to be $7 \pm 3\%$ from magnetic resonance images, small enough to affect the signal only slightly. For the case of the CRAZED signal, in addition to differences in magnetization density, the weighting also comes from differences in resonance frequency offsets [18]. In this bone–water system, the difference in magnetic susceptibility of the two phases is 2.28 ppm, enough to cause measurable effects [9]. In fact, significant differences are observed when comparing the y and z gradient curves in Fig. 4B. Also of interest is an apparent dip near the 2 mm correlation distance, however, we do not attribute this dip to any particular physical features. As will be seen later, the dip is a result of taking the magnitude of the complex signal.

The signal amplitude and phase depend on sample orientation with respect to the direction of the gradient
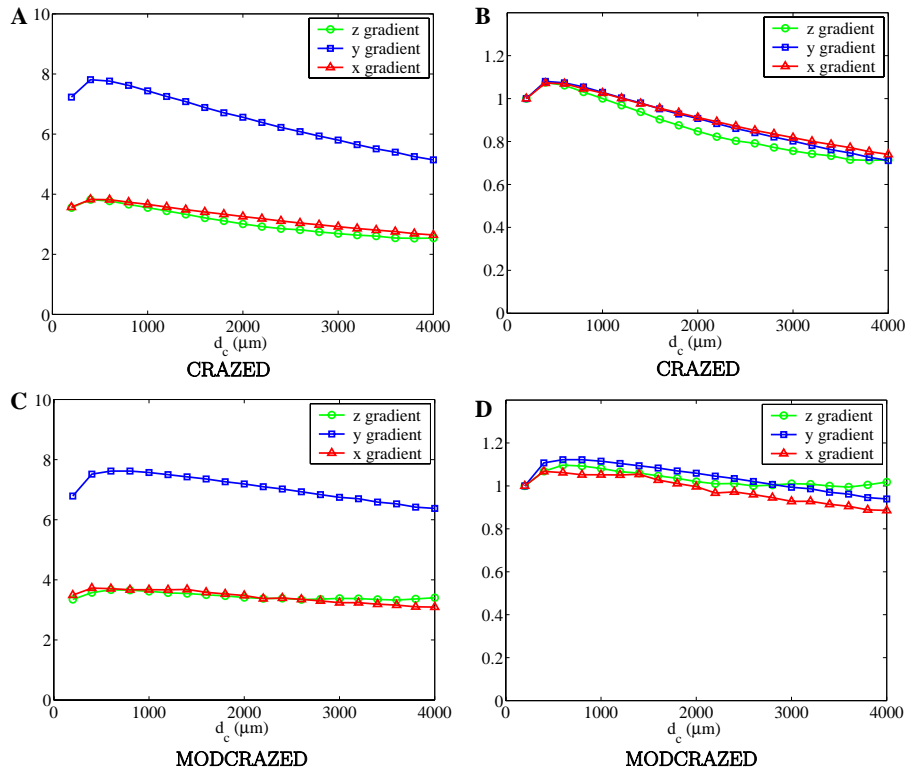
Fig. 3. Dependence of CRAZED and MODCRAZED signal intensities on correlation distance for a cylindrical water phantom (Setup #1). In (A) and (C), the raw magnitude is shown in absolute value. In (B) and (D), the curves are normalized to the first point to show relative changes. (See Fig. 2 for the coordinate system.) Parameters were $\tau = 30$ ms, TR = 5 s, $TE_{eff} = 200$ ms.

and applied field B_0. One way to characterize this relationship is by explicitly calculating the expected NMR signal as function of correlation distance, sample orientation, and gradient direction and comparing to actual measurements. We may do this using identical 3D maps of geometry and resonance frequency offsets. High-resolution spin echo anatomic images (128×128 matrix, 3 cm field of view, 1 mm thick contiguous slices) of the bone sample (see Fig. 5) were thresholded into a binary map and used as input for the three-dimensional indicator function $\chi(\mathbf{r})$. Fig. 5 readily shows the anisotropy of the sample, and therefore, of $\chi(\mathbf{r})$. Unlike $\chi(\mathbf{r})$, the anisotropy in $\omega(\mathbf{r})$ is more difficult to visualize because the map $\omega(\mathbf{r})$ also includes macroscopic fields over the field of view which reflect shimming conditions. The relevant gradients in $\omega(\mathbf{r})$ are those which occur over the correlation distance, rather than over the field of view. $\omega(\mathbf{r})$ was derived from two spin echo data sets: one regular acquisition and one with acquisition window delayed by 1 ms. The pixel-by-pixel complex ratio of the regular acquisition to the delayed acquisition gives a phase evolution proportional to the local resonance frequency offset in each pixel, and dividing by 1 ms gives the angular frequency [14], which then provides a three-dimensional map of resonance frequency offsets $\omega(\mathbf{r})$ as input for the calculation.

Fig. 4C is a plot of the calculated NMR signal—complex magnitude—versus correlation distance and gradient direction for measured maps of the three-dimensional indicator function $\chi(\mathbf{r})$ and resonance frequency offsets $\omega(\mathbf{r})$. We can see that the calculated signal (Fig. 4C) compares well to the measured signal (Fig. 4B) except at the longer correlation distances where the calculated signal is, in general, slightly lower. This discrepancy is due in part to the voxel size ($234\,\mu m \times 234\,\mu m \times 1$ mm) not being small enough to sharply resolve the indicator function along the boundaries of the trabecular network. We note that the z gradient curve lies below the y gradient curve for the range of d_c values considered; longer values of d_c were avoided because sample edge effects tend to dominate the measurement.

Aligning the specimen axis with the applied field B_0 results in a z gradient curve lying *above* the curves for gradients applied perpendicular to the bone axis (Fig. 6A). The data in Fig. 6A were acquired with $\tau = 6$ ms and so the rates of decay in the curves cannot be compared directly to the curves of Fig. 4 due to the different field strengths (4T versus 7T). Nevertheless, the general trends that govern the dependence on evolution time τ are expected to hold. Again, the calculated NMR signal of Fig. 6B satisfactorily reproduces the experimental
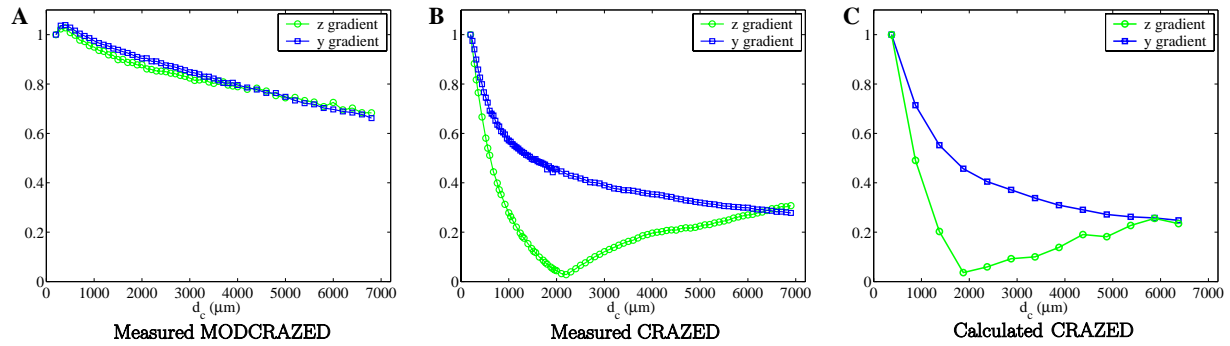
Fig. 4. Measured MODCRAZED (A) and CRAZED (B) signal versus correlation distance for z and y gradients for the bone axis perpendicular to B_0 with Setup #1. Parameters were $\tau = 15$ ms, TR = 5 s, TE$_{eff}$ = 200 ms. In (C) is the CRAZED signal calculated using the theoretical model. (See Fig. 2 for the coordinate system.) Plots show the magnitude of the complex signal.
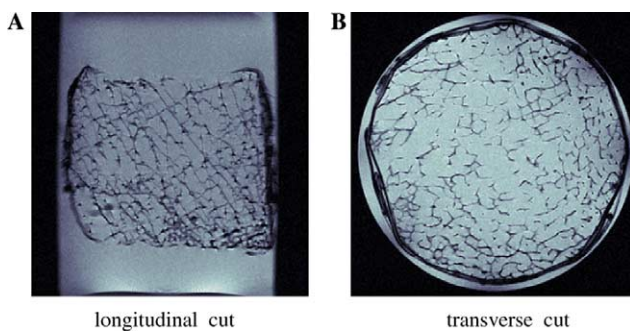

Fig. 5. Anisotropy of trabecular bone specimen as seen by comparing longitudinal (A) versus transverse (B) cuts (spin echo MRI with TE = 60 ms, TR = 1.6 s, 3 cm field of view, 256 × 256 matrix). The solid bone appears in black, while the water phase is in gray. The black rim around the sample is a thin wrapping layer of parafilm. The bone is approximately transversely isotropic where as the longitudinal section shows the dominant orientation to be from top left to bottom right, essentially along the direction of loading.

dependence on correlation distance for z and y gradients and for several values of the evolution time τ. Results are shown in Fig. 7; the x gradient is not shown on this graph as the results are similar to the y gradient. For both z and y gradients the signal decreases more sharply with increasing evolution time. We were unable to obtain accurate estimates above $\tau = 10$ ms with the data acquired at 7T because of the difficulty of modeling sharp magnetization gradients on this 128^3 grid which become important at long evolution times. Such limitations in numerical approximations of magnetization gradients on a finite grid have been encountered in previous studies [23]. A possible remedy is to use larger grid sizes or lower applied field strengths. Finally, we note that the dip in the y gradient curve shifts to smaller correlation distances as the evolution time is increased.

As mentioned previously, the dip arises when taking the magnitude of the complex signal. In Fig. 8 we plot the real (a) and imaginary (b) parts of the experimentally measured complex signal versus correlation distance, for z and y gradients, and for different evolution times. The shortest possible evolution time on this machine, with the pulse sequence of Fig. 1, was approximately 6 ms.
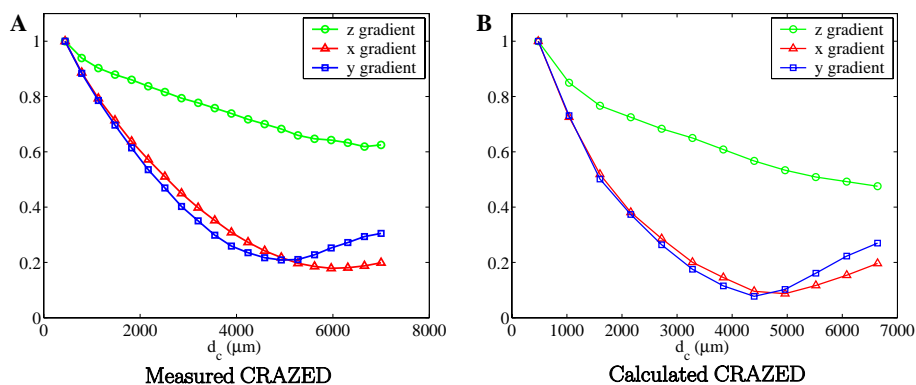
data in Fig. 6A, except for a slight underestimate at longer correlation distances, as observed previously.

Using the three-dimensional input maps $\chi(\mathbf{r})$ and $\omega(\mathbf{r})$ acquired with Setup #2 we calculated the signal

Fig. 6. NMR signal versus correlation distance and gradient direction for the bone axis parallel to B_0 (Setup #2). In (A) is the experimentally measured signal ($\tau = 6$ ms, TE$_{eff}$ = 212 ms) and in (B) is the calculated signal. Plots show the magnitude of the complex signal.
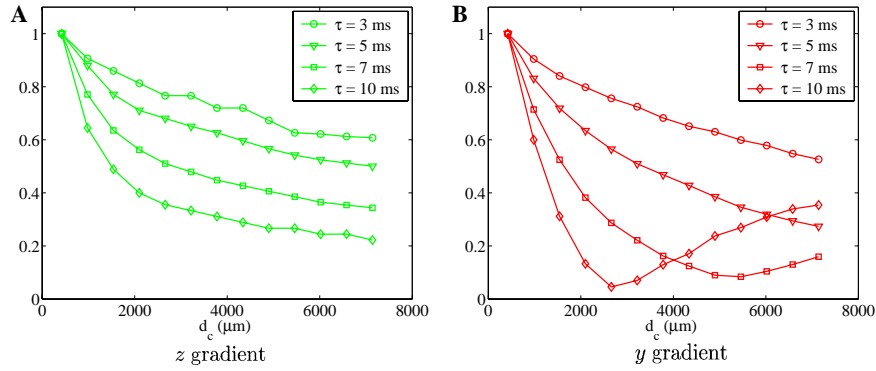
Fig. 7. Calculated CRAZED signal for z and y gradients at several τ values. Plots show the magnitude of the complex signal.

We first observe that the z gradient curves are approximately twice the amplitude of the y gradient curves, although this relationship is more ambiguous at long correlation distances. Second, we easily observe the trend which was verified in the previous numerical calculations, by which the curves decrease more rapidly with increasing evolution time τ.

For a CRAZED sequence [20] the single spin terms that contribute to the total signal accumulated phase factors $\exp(i(\omega_i - \omega_j)\tau)$, where $\omega_i - \omega_j$ is the resonance frequency difference between spins i and j. At short d_c the contributing spins are closer together and this difference is small. As d_c increases, the phase dispersion grows rapidly, and since the dispersion is the resonance
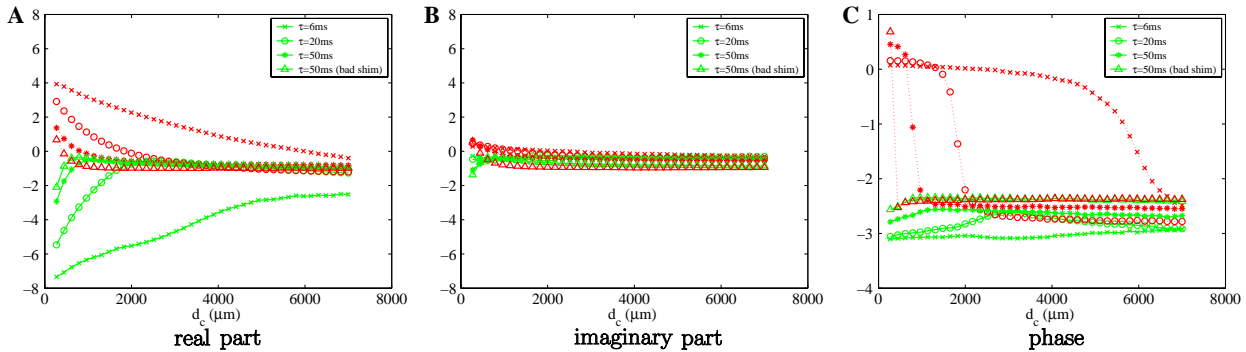

Fig. 8. Unnormalized raw amplitude (real, imaginary parts and phase angle) for the experimentally measured CRAZED signal at 7T (Setup #2), with the bone axis along B_0. Plots (A) and (B) are intensity versus correlation distance while (C) shows the phase angle. Several values of τ are shown for the case of z and y gradients (solid and dashed lines, respectively); curves for the x gradient are almost identical to the y gradient and are not shown.
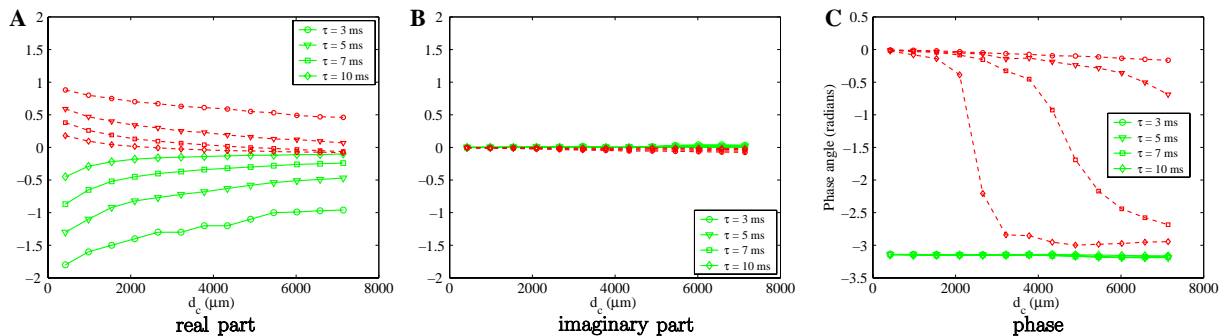

Fig. 9. Unnormalized raw amplitude (real, imaginary parts and phase angle) for the calculated CRAZED signal. Plots (A) and (B) are intensity versus correlation distance while (C) shows the phase angle. Several values of τ are shown for the case of z and y gradients (solid and dashed lines, respectively); curves for the x gradient are almost identical to the y gradient and are not shown.

frequency differences multiplied by the evolution time, the effects increase with τ.

Also noticeable is the phase of the signal as function of correlation distance (Fig. 8C) which exhibits a transition of roughly π radians in a narrow region of the graph, and this transition shifts to lower correlation distances as the evolution time is increased. The phase transition corresponds to the point where the real part of the signal for a y gradient crosses the zero line (dotted curves in Fig. 8A). The residual signal at correlation distances beyond the zero crossing reflects a significant degree of phase coherence in the volume-averaged long-range interactions which could be significantly different in other material geometries; however, the position of this transition is not correlated to any particular distance.

In Figs. 9A and B we show calculations of the complex signal versus correlation distance, real and imaginary parts for z and y gradients, and evolution times $\tau = 3, 5, 7$, and 10 ms. (For the reasons just mentioned previously, the maximum evolution time which could be used in the numerical calculations was approximately 10 ms.) In these theoretical calculations, we readily observe the expected 2:1 ratio in the signal amplitudes of the real part of the complex signal. The more rapid decay with correlation distance is observed at longer evolution times τ. In Fig. 9C the calculations reproduce the phase shift of π radians at specific correlation distances, the position of the transition is also seen to shift toward shorter d_c with increasing evolution time. Although only $\tau = 7$ and 5 ms were simulated, we can infer from the observed trend that the $\tau = 6$ ms curve would correspond roughly to the experimental data for the $\tau = 6$ ms curve in Fig. 8C.

4. Discussion

4.1. General trends

Several general trends emerge from our data. The fact that the signal decay curves decrease with increasing evolution time confirms that decay effects are due to gradients in the internal magnetic fields. Results from MODCRAZED experiments which show little dependence on correlation distance and gradient direction (Fig. 4A) confirm that the origin of these decays is from internal fields because the CRAZED and MODCRAZED sequences differ only by the contribution from resonance frequency offsets [18]. These gradients arise from the bone–water interface, where the jump in magnetic susceptibility is 2.28 ppm [12]. The dependence on correlation distance of the complex signal (real, imaginary, and phase) is verified quantitatively by our theoretical model. The trend for increasing τ is also verified, but we could only model short τ values due to lim-

itations introduced by the finite grid. Nevertheless, the CRAZED signal calculations are robust for the low internal field strengths investigated. These calculations would be less accurate for stronger internal fields, calling for larger grid sizes to be used.

4.2. Dependence on magnetic field gradient orientation

Another notable point concerns the dependence on gradient orientation, which proposes a possible methodology for non-invasively measuring the degree of structural anisotropy or the orientation of a material. Whether the bone axis z is oriented parallel (Setup #2) or perpendicular to B_0 (Setup #1) our results show that a gradient in the x or y direction gives the same answer, which makes sense since the trabecular structure is quasi-isotropic in the transverse plane (see Fig. 5). The curve for the z gradient lies either above or below the x and y gradient curves (compare Fig. 4B to 6A), depending on whether the sample is oriented parallel or perpendicular to the external field B_0. The lower curve for the sample aligned perpendicular to B_0 is consistent with elongated structures, such as cylinders, generating larger magnetic field perturbations when aligned perpendicular to the field direction. Thus, the position of the z curve relative to the x and y curves provides an indicator for the direction of the bone trabecular structure with respect to B_0. Moreover, the departure of the z gradient curve from the x or y curves is an indicator of the degree of anisotropy, as is evident when comparing these curves to the negligibly small differences observed in x, y, and z gradient curves for the sample of pure water (Fig. 3). These trends in the x, y and z gradient curves, combined with the ability to measure anisotropy, distinguish the DDF method from conventional spectral or T_2^* methods which generally show modulations following mechanical rotations of the sample but whose results strongly depend on extrinsic parameters such as voxel size. Further studies looking at various additional samples harvested from different skeletal locations would be needed to establish the robustness of such a measure beyond issues of inter-sample variability.

4.3. Optimization of the method for applications to materials

We envisage using this methodology based on indirect DDF measurements to assess the orientation of a material and its degree of anisotropy. However, the question remains as to which parameter (phase shift, initial slope or relative decrease of magnitude) would be better suited for this task. By fully characterizing a given material using experiments similar to the ones described in this article, it is likely that the curves will be sufficiently smooth so that only a few points along the curves need to be sampled. A protocol could, for example,

compare the relative decrease in signal magnitude for 2 or 3 different gradient directions. Relative decreases would account, to some extent, for the changing magnitude of internal fields from sample to sample, or due to material composition and applied field strength. In this manner, we believe that solutions to the inverse problem [4] may not be required. Preliminary work in relating iMQC signals from magnetic resonance images to physical parameters in trabecular bone has been carried out by Chin et al. [24].

A further complication in interpreting the data may arise from the sensitivity to magnet shimming. In our experiments, manual or automatic shimming produces little difference in the outcome. However, in cases of poor shimming we do observe significant discrepancies. Fig. 8 shows two curves for $\tau = 50$ ms, one acquired after automatic first order shimming, and the other with first order shims deliberately detuned to produce a free induction decay over the slice volume with about 10% of the amplitude obtained after an auto-shim. Finally, another marker of anisotropy could be the phase shift of π radians observed in Fig. 8C; however, this phase shift is also sensitive to shimming. In situations where NMR measurements are done outside the magnet (e.g., "ex situ NMR"), where the static field is highly inhomogeneous, the effects of the fringe field would need to be included in the analysis.

4.4. Extension to bone-marrow systems

These experiments serve as a first step toward the development of this technique for clinical applications. Work is underway in our laboratory to extend these studies to bone-marrow systems. Differences include a larger susceptibility shift at the bone-marrow interface (fat is less diamagnetic than water), multiple spectral lines and shorter relaxation times for the marrow phase. Shorter T_2 relaxation times result in lower signals; however, this effect is compensated partially by the shorter T_1 relaxation times which allow more averaging during the same time period using shorter repetition times. T_2 of the methylene protons in the fatty acyl chains is approximately 80 ms. T_1 in marrow is approximately 300 ms.

The multiple spectral lines do not represent a problem if the bulk signal is measured in the time domain at the center of the echo. However, multiple spin species complicate the numerical modeling; it will probably be necessary to use spectrally selective excitation pulses and frequency domain analysis of the signals. Diffusion would not be a problem since the self-diffusion coefficient of lipid protons is at least an order of magnitude lower than water. The results in future studies should be compared with independent measurements of structural anisotropy using, for example, the mean intercept length method or spatial autocorrelation analysis [13].

We believe that the methodology should ultimately be applicable in vivo.

5. Conclusion

In this study, we have investigated numerically and experimentally the dependence of the NMR CRAZED signal on correlation gradient strength and direction for a sample of demarrowed bone with the principal axis of the trabecular network oriented parallel and perpendicular to the applied field B_0. A simple linear model of the CRAZED signal provides calculations of the signal intensity that reproduce the general trends in the experimental data. These calculations accounted for differences in magnetization density and resonance frequency offsets and used three-dimensional maps of these parameters as input for the calculation. Our data suggest a possible method for non-invasively measuring material anisotropy based on effects from internal magnetic field gradients on the long-range dipolar interaction. The experiment essentially amounts to the indirect detection of the solid phase dipolar field by probing the liquid phase dipolar field.

References

[1] W. Warren, W. Richter, A. Hamilton Andreotti, B. Farmer, Generation of impossible cross-peaks between bulk water and biomolecules in solution NMR, Science 262 (1993) 2005–2009.

[2] P. Robyr, R. Bowtell, Measuring Patterson functions of inhomogeneous liquids using the nuclear dipolar field, J. Chem. Phys. 107 (1997) 702–706.

[3] C. Ramanathan, R. Bowtell, NMR imaging and structure measurements using the long-range dipolar field in liquids, Phys. Rev. E 66 (2002) 41201.

[4] L. Bouchard, W. Warren, Reconstruction of porous material geometry by stochastic optimization based on NMR measurements of the dipolar field, J. Magn. Reson. 170 (2004) 299–309.

[5] L. Bouchard, R. Rizi, W. Warren, Magnetization structure contrast based on intermolecular multiple-quantum coherences, Magn. Reson. Med. 48 (2002) 973–979.

[6] R. Bowtell, S. Gutteridge, C. Ramanathan, Imaging the long-range dipolar field in structured liquid state samples, J. Magn. Reson. 150 (2001) 147–155.

[7] W. Richter, M. Richter, W. Warren, H. Merkle, P. Andersen, G. Adriany, K. Ugurbil, Functional magnetic resonance imaging using intermolecular multiple-quantum coherences, Magn. Reson. Imaging 18 (2000) 489–494.

[8] L. Bouchard, H. Poptani, R. Rizi, J. Glickson, W. Warren, Intermolecular multiple-quantum coherence imaging of murine tumors depends on choice of dipolar correlation distance, in: Proceedings of the 11th Annual Meeting, International Society for Magnetic Resonance in Medicine, Toronto, 2003, p. 1112.

[9] W. Warren, S. Ahn, M. Mescher, M. Garwood, K. Ugurbil, W. Richter, R. Rizi, J. Hopkins, J. Leigh, MR imaging contrast enhancement based on intermolecular zero quantum coherences, Science 281 (1998) 247–252.

[10] Y. Lin, N. Lisitza, S. Ahn, W. Warren, Resurrection of crushed magnetization and chaotic dynamics in solution NMR spectroscopy, Science 290 (2000) 118–121.

[11] M. Ledbetter, I. Savukov, M. Romalis, Nonlinear amplification of small spin precession using long-range dipolar interactions, Phys. Rev. Lett. 94 (2005) 060801.

[12] J. Hopkins, F. Wehrli, Magnetic susceptibility measurement of insoluble solids by NMR: magnetic susceptibility of bone, Magn. Reson. Med. 37 (1997) 494–500.

[13] F. Wehrli, P. Saha, B. Gomberg, H. Song, P. Snyder, M. Benito, A. Wright, R. Weening, Role of magnetic resonance for assessing structure and function of trabecular bone, Top. Magn. Reson. Imaging 13 (2002) 335–356.

[14] H. Chung, S. Hwang, H. Yeung, F. Wehrli, Mapping of the magnetic-field distribution in cancellous bone, J. Magn. Reson. B 113 (1996) 172–176.

[15] S. Hwang, F. Wehrli, The calculation of the susceptibility-induced magnetic field from 3D NMR images with applications to trabecular bone, J. Magn. Reson. B 109 (1995) 126–145.

[16] L. Bouchard, Characterization of material microstructure using intermolecular multiple-quantum coherences, Ph.D. thesis, Princeton University, 2005

[17] G. Deville, M. Bernier, J. Delrieux, NMR multiple echoes observed in solid He-3, Phys. Rev. B 19 (1979) 5666–5688.

[18] S. Garrett-Roe, W. Warren, Numerical studies of intermolecular multiple quantum coherences: high-resolution NMR in inhomogeneous fields and contrast enhancement in MRI, J. Magn. Reson. 146 (2000) 1–13.

[19] T. Harrigan, R. Mann, Characterization of microstructural anisotropy in orthotropic materials using a second rank tensor, J. Mater. Sci. 19 (1984) 761–767.

[20] S. Lee, W. Richter, S. Vathyam, W. Warren, Quantum treatment of the effects of dipole–dipole interactions in liquid nuclear magnetic resonance, J. Chem. Phys. 105 (1996) 874–900.

[21] M. Garwood, L. DelaBarre, The return of the frequency sweep: designing adiabatic pulses for contemporary NMR, J. Magn. Reson. 153 (2001) 155–177.

[22] C. Ramanathan, R. Bowtell, Dynamics of the nuclear magnetic resonance COSY-revamped by asymmetric z-gradients (CRAZED) experiment, J. Chem. Phys. 114 (2001) 10854–10859.

[23] M. Ledbetter, I. Savukov, L. Bouchard, M. Romalis, Numerical and experimental studies of long-range magnetic dipolar interactions, J. Chem. Phys. 121 (2004) 1454–1465.

[24] C. Chin, X. Tang, L. Bouchard, W. Warren, F. Wehrli, Isolating quantum coherences in structural imaging using intermolecular double-quantum coherence MRI, J. Magn. Reson. 165 (2003) 309–314.